Supporting Information for

Fiber-shaped sensor constructed by coaxial wet-spinning for dual-mode sensing

Duixin Ma[1], Huayang Fang[1], Jianping Sun[1], Tao Jiang[2]**

[a]State Key Laboratory of Featured Metal Materials and Life-cycle Safety for Composite Structures, School of Resources, Environment and Materials, Guangxi University, Nanning 530004, China

[b]School of Journalism and Cultural Communication, Guangxi University of Finance and Economics, Nanning, Guangxi 530004, China

E-mail: jpsun@gxu.edu.cn, 443133847@qq.com.

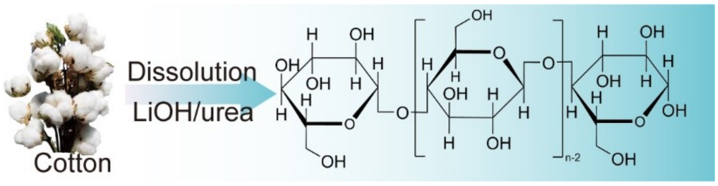

Figure S1. Schematic diagram of cellulose dissolution by alkali urea system.

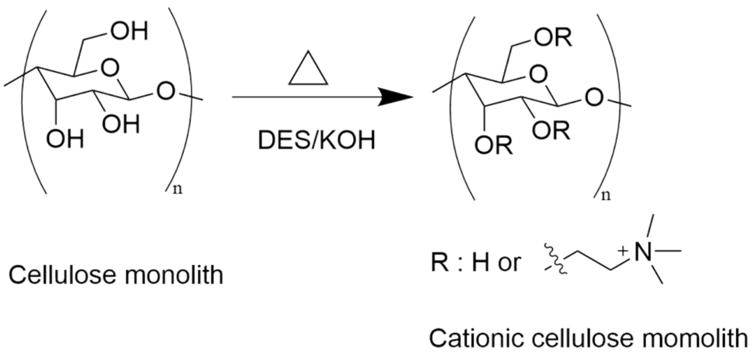

Figure S2. Schematic diagram of the functionalization of cellulose monolith by CCC/urea deep eutectic solvent.

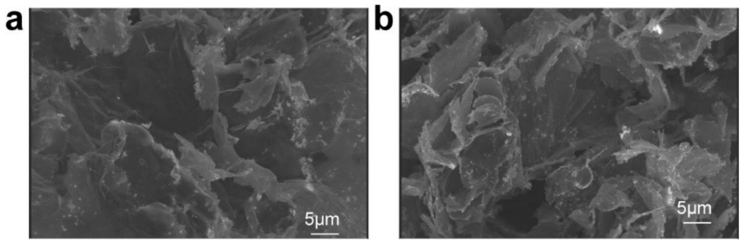

Figure S3. Morphology of cellulose powder (a) before and (b) after DES modification.

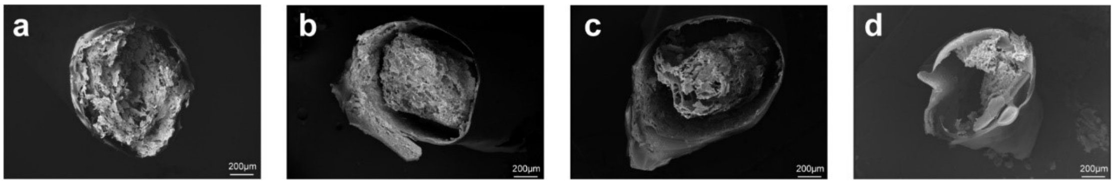

Figure S4. SEM of MCC fibers. (a-d) Cross-sectional morphology of MCC-(1, 3, 9, 12).

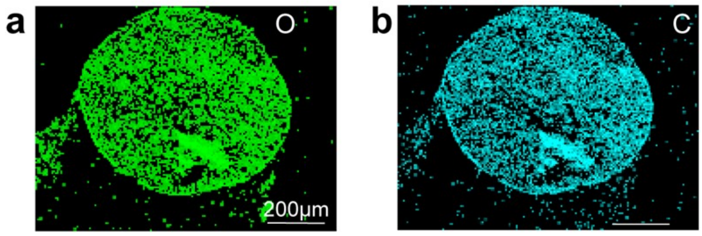

Figure S5. EDS mapping of the skin-core MCC-6 aerogel fibers.

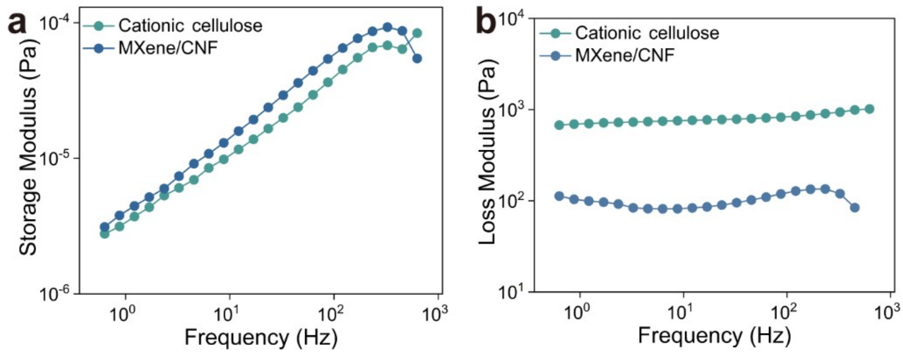

Figure S6. Viscosity of spinning solution with Cellulose and MXene/CNF. a-b) The curve of storage modulus (G') and loss modulus (G'') of Cellulose and MXene/CNF with frequency.

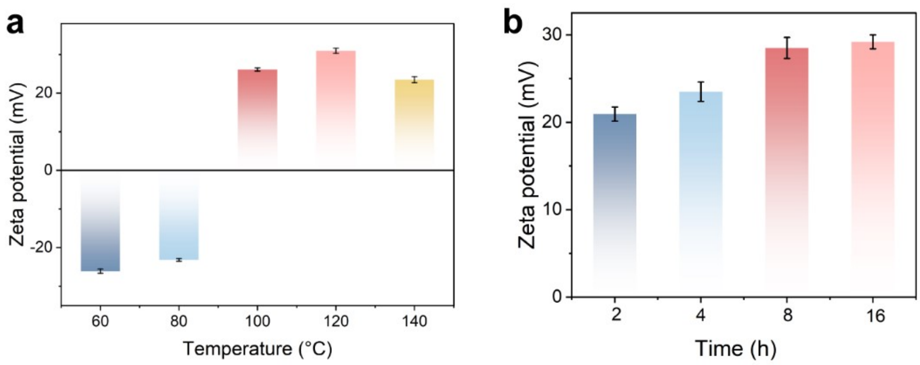

Figure S7. a-b) Zeta potential of cellulose at different treatment temperatures and times, respectively.

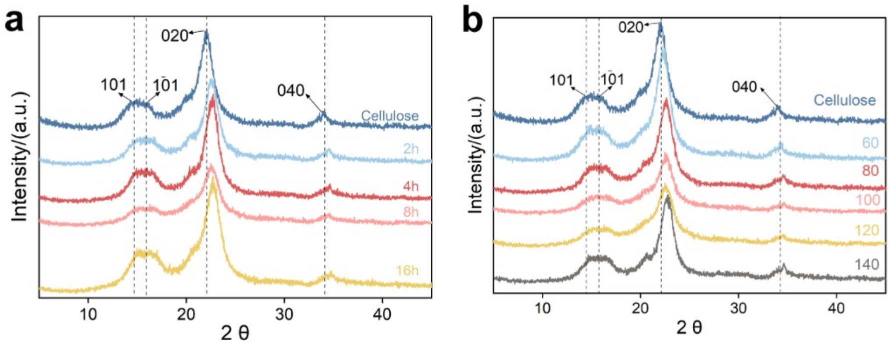

Figure S8. XRD analysis of cellulose and cationized MCC-6 before and after DES modification. a) Effect of different DES modification times on cellulose crystallinity. b) Effect of different DES modification temperatures on cellulose crystallinity.

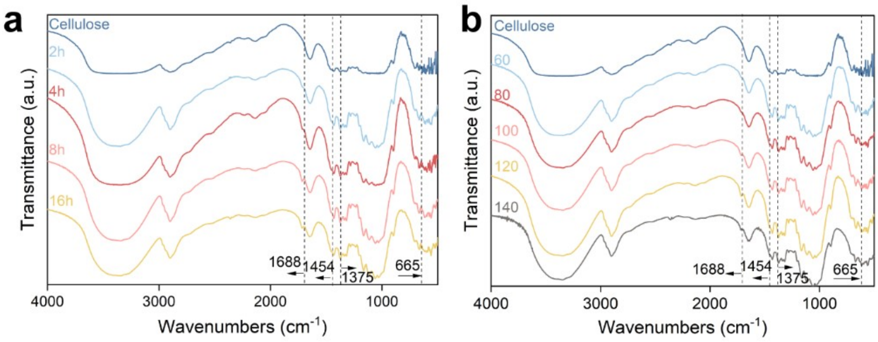

Figure S9. FTIR analysis of cellulose and cationized MCC-6 before and after DES modification. a) Effect of different DES modification times on cellulose crystallinity. b) Effect of different DES modification temperatures on cellulose crystallinity.

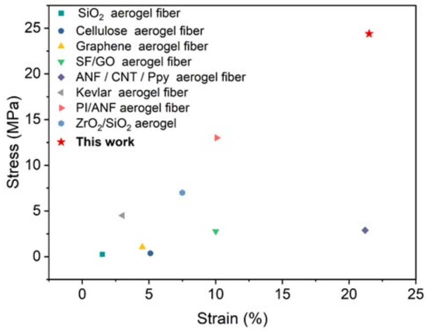

Figure S10. Comparison of mechanical properties of MCC-6 with other literature[1-8].

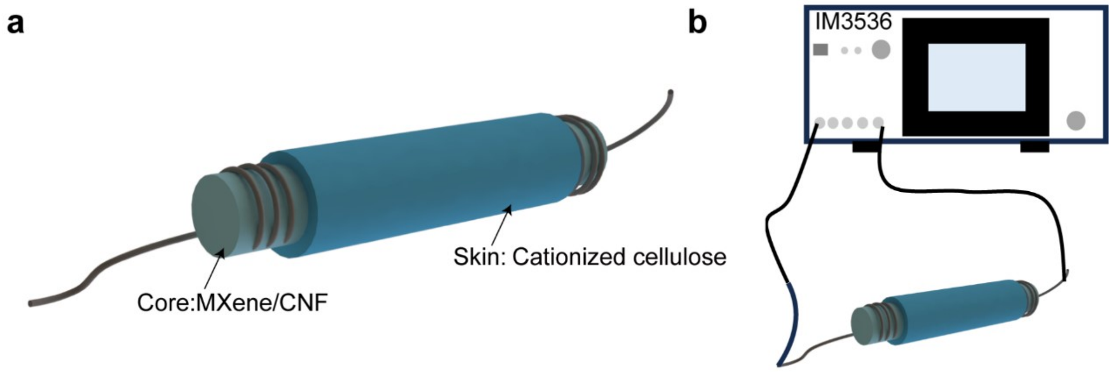

Figure S11. Schematic diagram of (a) the wiring for the fiber sensor in pressure sensing and (b) performance test setup for pressure sensing.

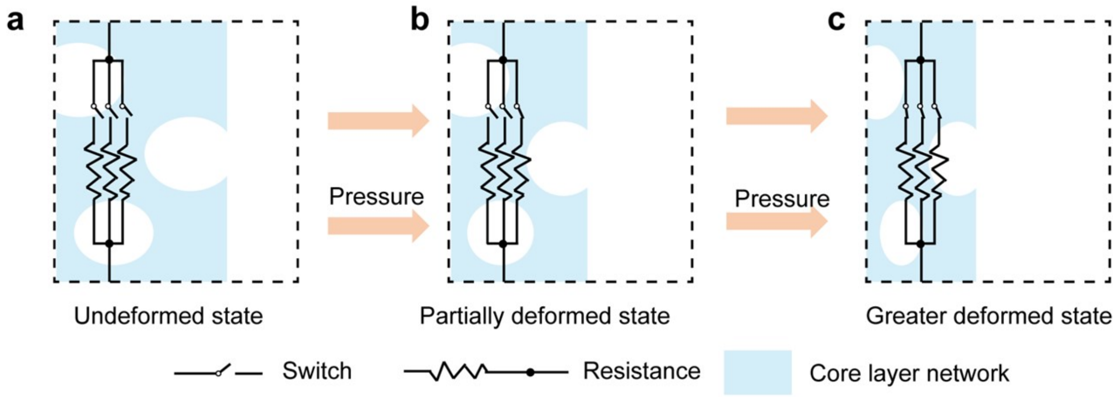

Figure S12. Equivalent circuit diagrams reflecting changes in resistance with deformation: (a) no deformation; (b) partial deformation; (c) greater deformation.

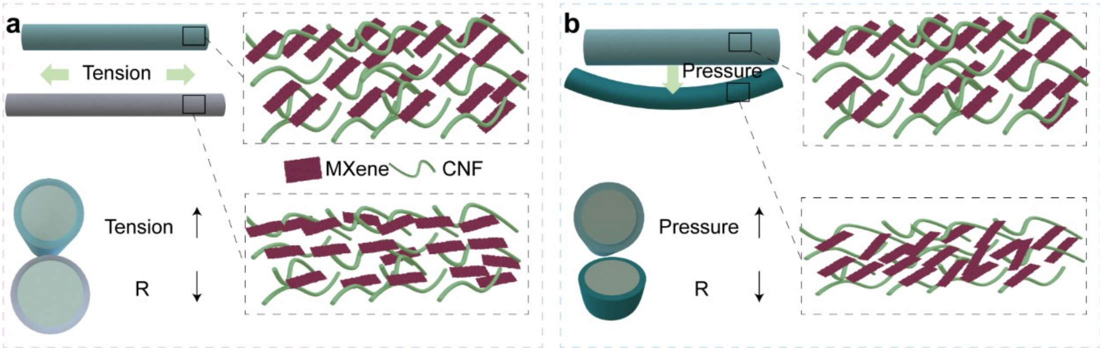

Figure S13. Schematics of the sensing principle of the MCC-6 sensor under (a) stretching and (b) compressive deformation.

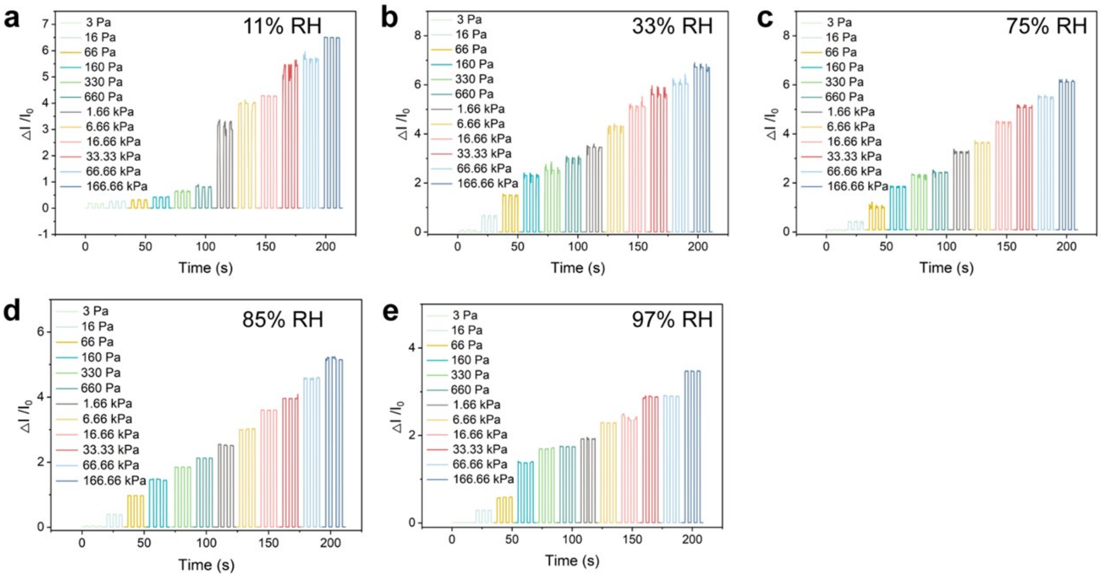

Figure S14. Current-time (*I-T*) plots of the MCC-6 fiber under various pressures at a constant humidity level. a-e) *I-T* plots of the MCC-6 fiber under various pressures at (a) 11% RH, (b) 33% RH, (c) 75% RH, (d) 85% RH, and (e) 97 % RH.

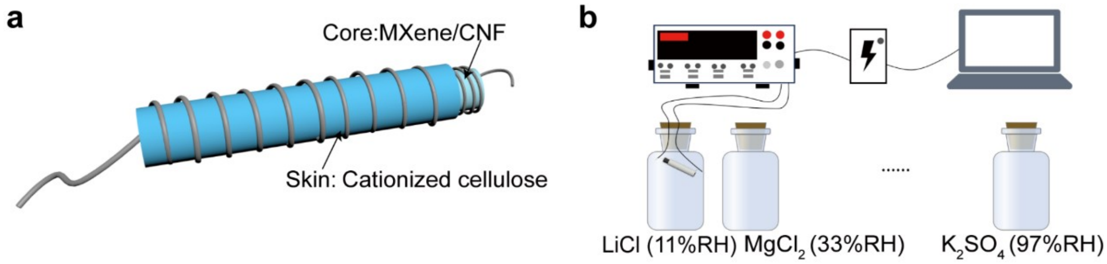

Figure S15. Schematic diagram of (a) the wiring for the fiber sensor in humidity sensing and (b) performance test setup for humidity sensing.

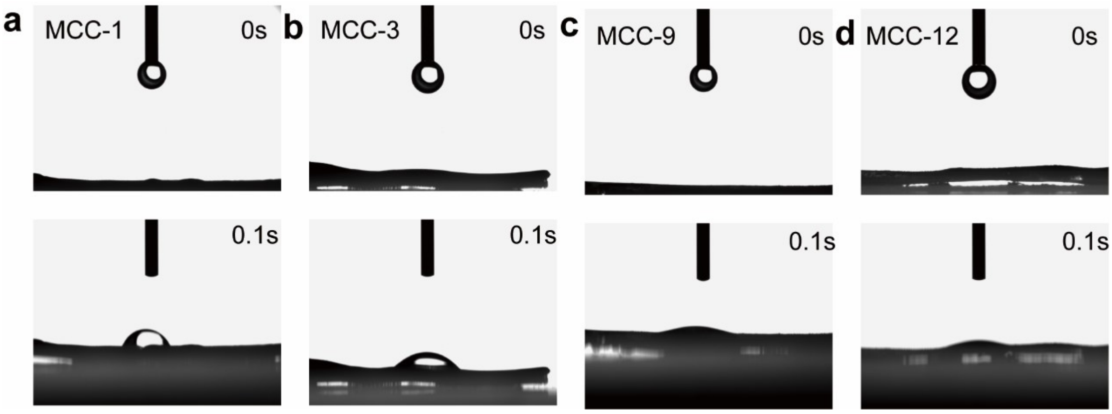

Figure S16. The water contact angle of the MCC humidity sensor. a-d) Water contact angle of the MCC-(1, 3, 9, 12) humidity sensor.

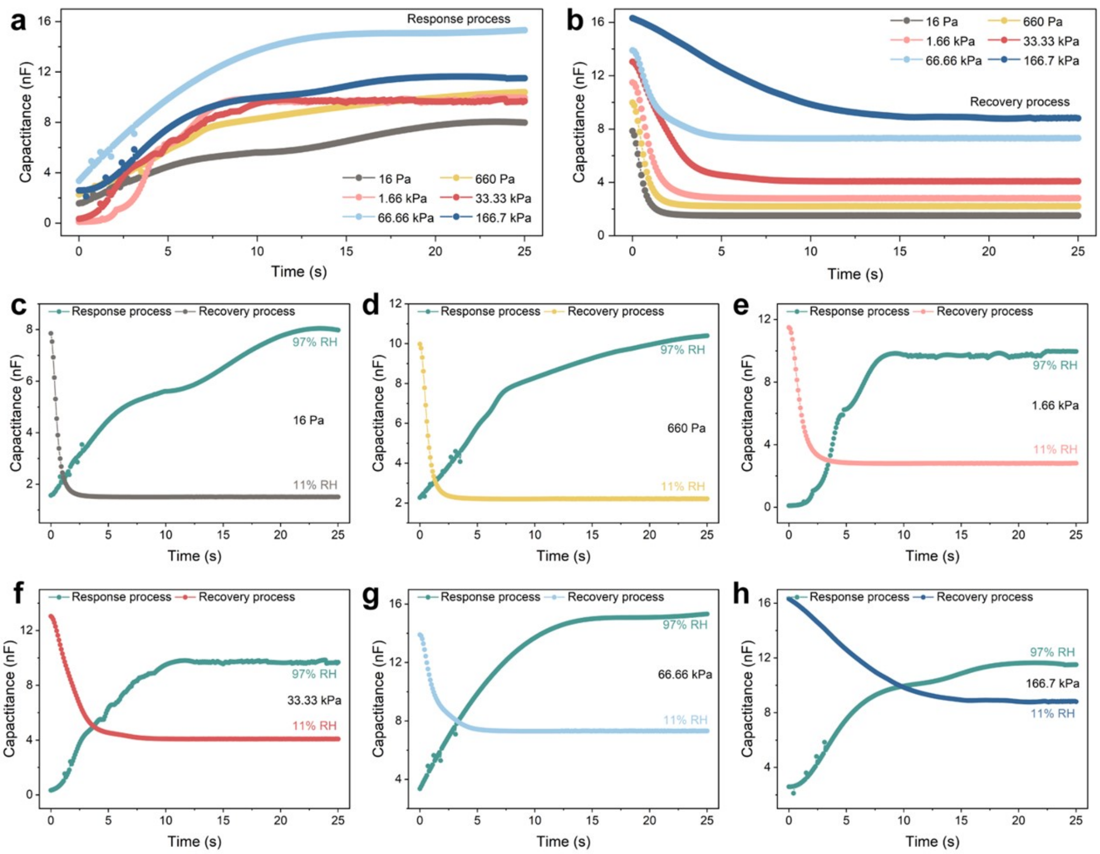

Figure S17. Capacitive response and recovery characteristics of MCC-6 to humidity changes under different pressure conditions. a) Capacitive response of the MCC-6 to humidity changes at a constant 0.016-166.7 kPa pressure. b) Recovery characteristics of the MCC-6 to humidity changes at a constant 0.016-166.7 kPa pressure. c-h) Capacitive response and recovery characteristics of the MCC-6 under various humidity at 0.016 kPa, 0.66 kPa, 1.66 kPa, 33.33 kPa, 66.66 kPa, 166.7 kPa pressure.

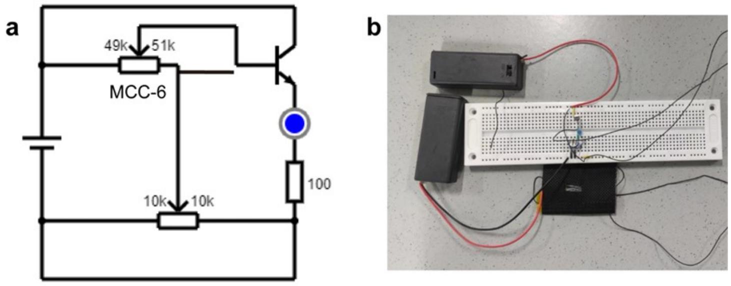

Figure S18. Photograph of the circuit used to monitor the condition of the lumbar spine. a) a circuit diagram consisting of a 6V electric power source, the MCC fabric sensor, an NPN-type transistor, a rotary variable resistor, a blue light-emitting diode (with a driving voltage of 1.8V). b) digital photograph of the circuit.

A · -	J · - -	S · · ·
B - · ·	K - · -	T -
C - · - ·	L · - · ·	U · · -
D - · ·	M - -	V · · · -
E ·	N - ·	W · - -
F · · - ·	O - - -	X - · - -
G - - ·	P · - -	Y - · - -
H · · · ·	Q - - · -	Z - - · ·
I · ·	R · - ·	

Figure S19. Morse code cross reference table.

Figure S20. Wrist flexion current display on a smartphone.

Table S1. Comparison of the MCC-6 fiber with previous reports.

Sample	Response/ Recovery time(ms)	Detection limit (Pa)	Sensitivity (kPa^{-1})	Ref
EEG/textile electrodes	373/500	160	**0.16** (0.169-1 kPa)，**0.05**(1-10 kPa)	9
CA/PPy (CAP) aerogel	112/98	0.5	**1.08** (0-3.5 kPa)，**0.76** (3.5-9 kPa)，**0.56** (9-15.5 kPa)，**0.49** (15.5-20 kPa)	10
PU/RGO sponge	750/750	5	**17.65**(0.005-3.20 kPa)，**11.51** (3.2-6.2 kPa)，**2.82**(6.2-19.4 kPa)kPa，**8.61**(19.4-30.4 kPa)	11
graphene/SWNTs paper	380/60	30	**12.07**(0.03-0.6 kPa)，**4.3**(0.6-60.4 kPa)	12
MXene Spheres	34/56	140	**3.14**(0.14-22.22 kPa)，**0.22** (22.22-140 kPa)	13
Ag NW/PU fiber	18/19	5	**16.7**(0.005-0.05 kPa)，**0.17**(0.05-1 kPa)	14
MX/rGO	130/140	1.27	**1.24**(0.0012-11 kPa)，**0.12**(11-100 kPa)	15
MXene/ANFs film	100/160	0.5	**7**(0.005-10 kPa)，**10.52**(10-40 kPa)，**4**(40-80 kPa)，**16.73**(80-100 kPa)	16
P-rGO@WS aerogel	160/200	180	**0.0493**(0.18-5 kPa)，**0.00075**(5-50kPa)	17
PAAm / PVA hydrogel	180/170	9	**2.27**(0.009-0.5 kPa)，**0.8**(0.5-2kPa)，**0.021**(2-5kPa)	18
MCC-6	50/55	3	**120**(0.33-3.33kPa)，**6**(3.33-50kPa)，**0.5**(50-233.33kPa)	**This work**

References

1. Y. Du, X. Zhang, J. Wang, Z. Liu, K. Zhang, X. Ji, Y. You and X. Zhang, *ACS nano*, 2020, **14**, 11919-11928.
2. J. Huang, J. Li, X. Xu, L. Hua and Z. Lu, *ACS nano*, 2022, **16**, 8161-8171.
3. G. Li, G. Hong, D. Dong, W. Song and X. Zhang, *Advanced materials*, 2018, **30**, 1801754.
4. M. Li, Z. Wu, X. Chen, F. Gan, C. Teng, X. Li, J. Dong, X. Zhao and Q. Zhang, *Chemical Engineering Journal*, 2024, **486**, 150255.
5. Q. Li, Z. Yuan, C. Zhang, S. Hu, Z. Chen, Y. Wu, P. Chen, H. Qi and D. Ye, *Nano Letters*, 2022, **22**, 3516-3524.
6. Z. Liu, J. Lyu, Y. Ding, Y. Bao, Z. Sheng, N. Shi and X. Zhang, *ACS nano*, 2022, **16**, 15237-15248.
7. Z. Wang, H. Yang, Y. Li and X. Zheng, *ACS applied materials & interfaces*, 2020, **12**, 15726-15736.
8. M. Yang, Y. Ding, Z. Chen, Q. Wu, L. Liu, T. Liu, M. Li, K. Xu, L. Le and L. Yang, *Journal of the American Ceramic Society*, 2024.
9. N. Li, S. Gao, Y. Li, J. Liu, W. Song and G. Shen, *Nano Research*, 2023, **16**, 7583-7592.
10. S. Wang, W. Meng, H. Lv, Z. Wang and J. Pu, *Carbohydrate Polymers*, 2021, **270**, 118414.
11. W. Cao, Y. Luo, Y. Dai, X. Wang, K. Wu, H. Lin, K. Rui and J. Zhu, *ACS Appl. Mater. Interfaces*, 2023, **15**, 3131-3140.
12. Y. Wei, X. Shi, Z. Yao, J. Zhi, L. Hu, R. Yan, C. Shi, H.-D. Yu and W. Huang, *npj Flexible Electron.*, 2023, **7**, 13.
13. Z. Yang, S. Lv, Y. Zhang, J. Wang, L. Jiang, X. Jia, C. Wang, X. Yan, P. Sun, Y. Duan, F. Liu and G. Lu, *Nano-Micro Lett.*, 2022, **14**, 56.
14. Y. Dai, Y. Song, Y. Zhou, M. Zhou, H. Song, H. Wang, R. Wang, J. He, K. Qi and K. Ou, *ACS Appl. Mater. Interfaces*, 2023, **15**, 11244–11258.
15. N. Yang, H. Liu, X. Yin, F. Wang, X. Yan, X. Zhang and T. Cheng, *ACS Appl. Mater. Interfaces*, 2022, **14**, 45978-45987.
16. C.-Y. Huang, G. Yang, P. Huang, J.-M. Hu, Z.-H. Tang, Y.-Q. Li and S.-Y. Fu, *ACS Appl. Mater. Interfaces*, 2023, **15**, 3476–3485.
17. W. Huang, H. Li, L. Zheng, X. Lai, H. Guan, Y. Wei, H. Feng and X. Zeng, *Chem. Eng. J.*, 2021, **426**, 130837.
18. Y. Kim, J. B. Park, Y. J. Kwon, J.-Y. Hong, Y.-P. Jeon and J. U. Lee, *J. Mater.*

Chem. C, 2022, **10**, 9364-9376.